The Planetary Science Journal, 3:131 (13pp), 2022 June https://doi.org/10.3847/PSJ/ac66e9


# Model of Double Asteroid Redirection Test Impact Ejecta Plume Observations

Andrew F. Cheng[1], S. D. Raducan[2], Eugene G. Fahnestock[3], Elisabetta Dotto[4], Vincenzo Della Corte[5], and Angela M. Stickle[1]
[1] JHU/APL, MD, USA; andrew.cheng@jhuapl.edu
[2] Univ. of Bern, Switzerland
[3] JPL, CA, USA
[4] INAF-OA, Rome, Italy
[5] INAF-IAPS, Rome, Italy
*Received 2021 October 4; revised 2022 March 21; accepted 2022 April 6; published 2022 June 2*

## Abstract

The Double Asteroid Redirection Test (DART) spacecraft will impact the moon Dimorphos of the [65803] Didymos binary in order to demonstrate asteroid deflection by a kinetic impactor. DART will measure the deflection by using ground-based telescopic observations of the orbital period change of Didymos and will carry the Light Italian CubeSat for Imaging of Asteroids (LICIACube) cubesat, which will perform a flyby of Didymos about 167 s after the DART impact, obtaining images of the DART impact ejecta plume. LICIACube images showing the ejecta plume spatial structure and temporal evolution will help determine the vector momentum transfer from the DART impact. A model is developed for the impact ejecta plume optical depth, using a point-source scaling model of the DART impact. The model is applied to expected LICIACube plume images and shows how plume images enable characterization of the ejecta mass versus velocity distribution. The ejecta plume structure, as it evolves over time, is determined by the amount of ejecta that has reached a given altitude at a given time. The evolution of the plume optical depth profiles determined from LICIACube images can distinguish between strength-controlled and gravity-controlled impacts, by distinguishing the respective mass versus velocity distributions. LICIACube plume images discriminate the differences in plume structure and evolution that result from different target physical properties, mainly the strength and porosity, thereby allowing inference of these properties to improve the determination of DART impact momentum transfer.

*Unified Astronomy Thesaurus concepts:* Near-Earth objects (1092); Close encounters (255)

## 1. Introduction

The NASA Double Asteroid Redirection Test (DART) mission will target the moon Dimorphos of the [65803] Didymos binary asteroid system in order to demonstrate asteroid deflection by kinetic impact, modifying the moon's orbit through momentum transfer. DART launched on 2021 November 24 and will impact Dimorphos on 2022 September 26. The change in the moon's orbit period from the impact will be observed by ground-based telescopes to confirm and measure the amount of deflection. The DART impact is required to cause at least a 73 s change in the binary orbit period, and DART is required to determine the momentum transfer efficiency ($\beta$) of the impact and characterize the impact outcomes. The DART observations and investigation tasks to meet these requirements are discussed by Rivkin et al. (2021) and previously summarized by Cheng et al. (2018). The DART mission as a kinetic impactor experiment was discussed by Cheng et al. (2016), who predicted changes in the binary orbit period, eccentricity and inclination and who presented an analytic, point-source scaling law model of the DART impact to predict the momentum transfer to Dimorphos. The analytic expression for momentum transfer (Cheng et al. 2016, Equation (9)) was tested by Raducan et al. (2019), who found agreement with numerical simulations within ~10%.

The European Space Agency Hera mission will rendezvous with the Didymos system about 4 yr after the DART impact. Hera will measure the mass of Dimorphos and determine the dimensions of the DART impact crater, and it will study the binary system dynamics as well as internal structure (Michel et al. 2016, 2018). The members of the Hera mission team and the DART mission team together comprise the Asteroid Impact & Deflection Assessment (AIDA) collaboration.

The 6U Light Italian CubeSat for Imaging of Asteroids (LICIACube; Dotto et al. 2021) was added to the DART mission in 2018. LICIACube, contributed to the DART mission by the Italian Space Agency (ASI), will be carried by DART to Didymos and deployed to make a separate flyby of Didymos, with the closest approach time delayed by 167 s from the DART impact. LICIACube will image the impact ejecta plume and study its evolution, and it will image the nonimpact hemisphere of Dimorphos and Didymos. These observations make important contributions to the estimation of momentum transfer (Cheng et al. 2020).

This paper will develop a model of the DART impact ejecta plume opacity as observed by LICIACube from its flyby trajectory, extending the previous plume model developed by Cheng et al. (2020), which showed how plume images can discriminate the differences in plume structure and evolution that result from different target physical properties, and thereby distinguish between strength-controlled and gravity-controlled impacts. The Cheng et al. (2020) model calculated the optical depth profiles along a specific one-dimensional cut through a LICIACube plume image, the image line connecting the impact site with the intersection of the LICIACube trajectory and the

**Table 1**
DART Kinetic Impact and LICIACube Flyby Mission Design

| | | |
|---|---|---|
| DART | Launch Date | 2021 Nov 24 |
| | Arrival Date | 2022 Sep 26 |
| | Arrival Relative Speed | 6.145 km $s^{-1}$ |
| | Maximum Earth Distance | 0.19 au |
| | Earth Distance at Impact | 0.0757 au |
| | Solar Distance at Impact | 1.046 au |
| | Arrival Solar Phase Angle | 59.°5 |
| | Impact Angle to Binary Orbit Velocity | 166° |
| LICIACube | Release from DART | 10 days before DART impact |
| | Flyby Speed Relative to Didymos | 6.145 km $s^{-1}$ |
| | Closest Approach Distance to Didymos | 51.2 km |
| | Closest Approach Delay from DART Impact | 167 s |
| | Time for which LEIA images are <5 m $px^{-1}$ | 63.7 s |

plane of sky at Dimorphos. The present work extends the Cheng et al. (2020) model to calculate optical depth profiles along different image lines covering the full two-dimensional plume images.

The LICIACube flyby trajectory and the DART impact trajectory are summarized in Table 1. DART will impact Dimorphos at 6.145 km $s^{-1}$ on 2022 September 26, in a direction approximately opposite, at an angle of 166°, to the orbital velocity. The LICIACube flyby speed is approximately the same as the DART impact speed, to within 5 m $s^{-1}$. The LICIACube closest approach distance to Didymos will be 51.2 km, and the time delay of closest approach after the DART impact will be 167 s, optimizing LICIACube imaging of ejecta plume structure and evolution (Dotto et al. 2021).

The LICIACube imaging payload consists of two cameras (Dotto et al. 2021) whose characteristics are summarized in Table 2. First is the LICIACube Explorer Imaging for Asteroid (LEIA) camera, which is a monochrome imaging system with a 7.56 cm aperture, $f/3$ telescope. The LEIA field of view (FOV) is $2.^{\circ}9 \times 2.^{\circ}9$, and the instantaneous field of view (IFOV) is 25 $\mu$rad $pixel^{-1}$. Second is the LICIACube Unit Key Explorer (LUKE) camera, which is an RGB color imager with a wider FOV of $9.^{\circ}2 \times 4.^{\circ}9$ and IFOV of 78 $\mu$rad $px^{-1}$. The best image resolution with LEIA near closest approach, occurring 167 s after the DART impact, corresponds to a ground sampling distance at Dimorphos of 1.4 m $px^{-1}$, while LUKE achieves a best resolution of 4 m $px^{-1}$.

The width of the LEIA FOV at the distance of Didymos is 2.6 km near closest approach. Ejecta released at a typical speed of 5 m $s^{-1}$ (Jutzi & Michel 2014) will have reached an altitude ~840 m at that time, and even faster ejecta remain within the LEIA FOV. The wider FOV of LUKE measures 8.2 by 4.4 km at the distance of Didymos near closest approach. The fields of view of both LUKE and LEIA are wide enough to include both Didymos and Dimorphos even near closest approach (Didymos diameter 780 m; Dimorphos diameter 164 m; orbital semimajor axis 1.2 km; Dotto et al. 2021 and Rivkin et al. 2021).

This paper will focus on LICIACube observations of the ejecta plume structure and evolution and implications for DART determination of momentum transfer efficiency $\beta$. The

**Table 2**
LICIACube Imagers

| Imager | LEIA | LUKE |
|---|---|---|
| IFOV | 25 $\mu$rad $px^{-1}$ | 78 $\mu$rad $px^{-1}$ |
| FOV | $2.^{\circ}9 \times 2.^{\circ}9$ | $9.^{\circ}2 \times 4.^{\circ}9$ |
| Spectral bandpass | Panchromatic 400–900 nm | RGB Bayer filter |

definition of $\beta$ applicable to DART is given in Appendix A, consistent with the definition introduced by Feldhacker et al. (2017) and used by Cheng et al. (2020) and Rivkin et al. (2021). The $\beta$ definition [A2] shows explicitly the importance of the unit vector $\boldsymbol{n}$, the direction of the net ejecta momentum, which is an observable that can be determined from LICIACube plume images. The $\beta$ definition [A3] is reexpressed (Rivkin et al. 2021) to show the contributions of the local surface normal vector at the impact site (also an observable to be determined from DART images) and the direction of the binary orbital motion.

To support the determination of the plume momentum direction from LICIACube images, a model of the plume structure and opacity is needed for the entire plume as seen in the images. The present paper develops such a model, to calculate optical depth profiles along arbitrary image lines parallel to the single line considered by Cheng et al. (2020), which is $z = 0$. Parameters $z_0$ and $b$, which are distances measured in the plane of sky at Dimorphos (see Figure 1), are used because they directly convert to pixel distances seen in LICIACube plume images.

## 2. Impact Ejecta Plume as Observed by LICIACube

This paper develops a model for the ejecta plume opacity as imaged by LICIACube during its flyby of Didymos (Dotto et al. 2021). LICIACube will point its imagers to Didymos autonomously throughout the flyby, and images will be acquired by both LICIACube cameras during all of the distant approach, closest approach, and early departure phases of the flyby.

Figure 1 shows the viewing geometry for plume imaging by LICIACube from its flyby trajectory, in distant approach. The DART impact site is at the coordinate origin, and the $y$-axis is the axis of the ejecta cone. LICIACube is at position ($x_s$, $y_s$, 0), on a flyby trajectory in the $x$–$y$ plane such that $x_s = 51.2$ km and $y_s$ decreases with time. As LICIACube follows DART on almost the same trajectory, LICIACube on distant approach viewing Didymos is also viewing roughly along the plume axis from great distance at a solar phase angle near 60°. These initial images will be said to be obtained from inside the ejecta cone. In these initial images, each line of sight through the plume intersects the cone once. The optical depth is calculated as in Cheng et al. (2020) by an integration along the line of sight through the cone intersection. As sketched in Figure 1, the ejecta form a hollow cone, where the cone walls are considered to have negligible thickness in the present model. If the cone is extended to infinity, above altitudes that may actually be reached by ejecta, the intersection of the LICIACube trajectory with the ejecta cone occurs at the point labeled cone crossing.

LICIACube passes through the cone crossing before it reaches closest approach. After cone crossing and near closest approach, LICIACube images are obtained from outside the

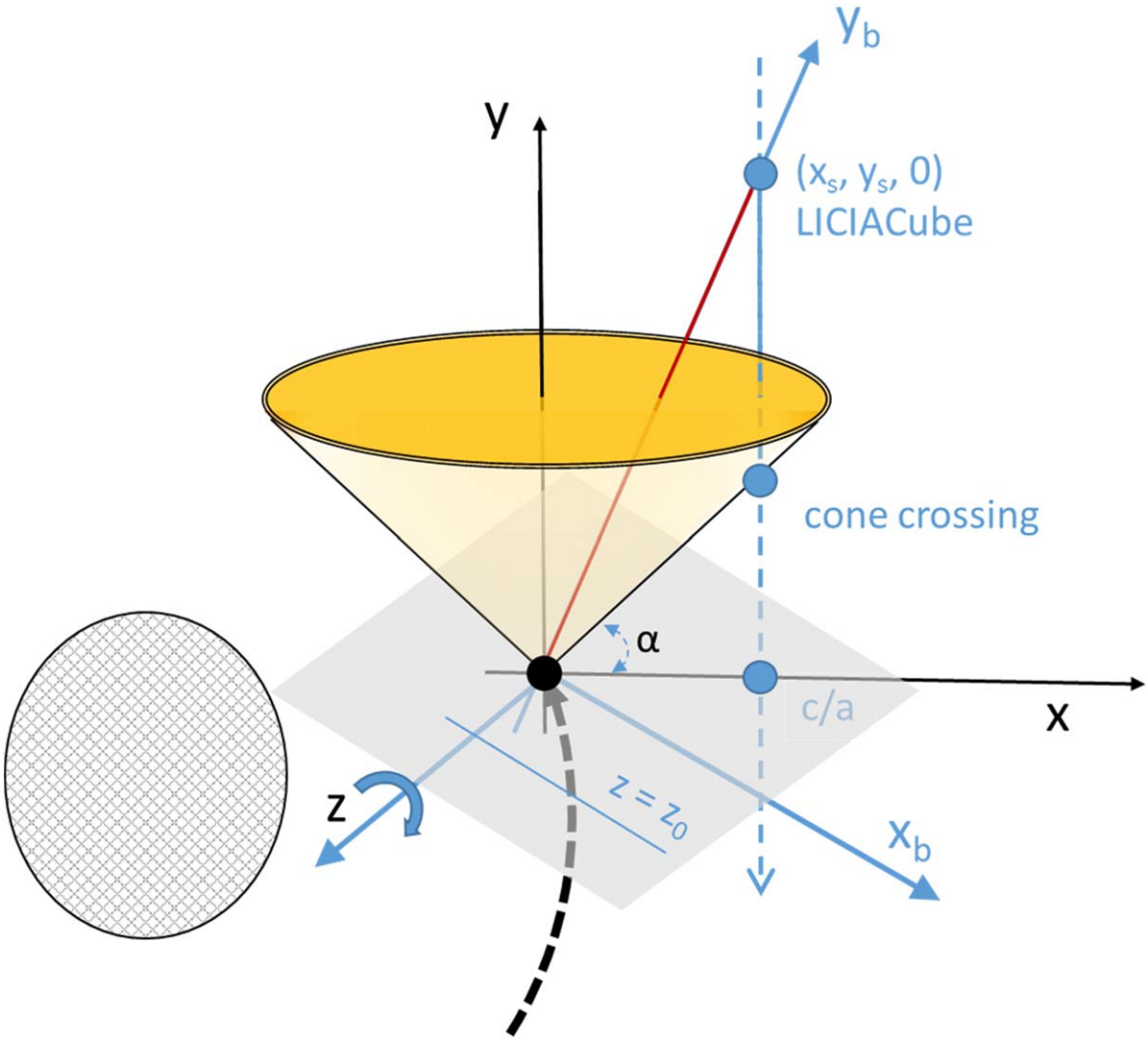


**Figure 1.** DART impact on Dimorphos is at the origin of Cartesian coordinates ***x*–*y*–*z***. LICIACube trajectory is dashed blue line in the ***x*–*y*** plane. LICIACube position is $(x_s, y_s, 0)$ in distant approach. Didymos is crosshatched oval to left, and the Dimorphos orbit is dashed black arrow. The line of sight to the Dimorphos impact site is the red line defining the $\boldsymbol{y_b}$ axis. The plane of sky at Dimorphos seen from LICIACube is the $\boldsymbol{x_b}$–$\boldsymbol{z}$ plane (shaded), which is rotated around $\boldsymbol{z}$ from ***x*–*z***. Optical depth profiles calculated by Cheng et al. (2020) for image lines at constant $z = 0$. Optical depth profiles for image lines at constant $z = z_0$ in the plane of sky given here. The DART impact ejecta cone is shown in yellow; it is a hollow cone with negligibly thin walls. The cone axis is $\boldsymbol{y}$, with ejecta angle $\alpha$. The ejecta cone crossing and the closest approach $c/a$ of LICIACube trajectory are indicated by blue dots.

cone, and now each line of sight through the plume intersects the cone twice. The optical depth is now calculated by summing the contributions from the two cone intersections. These images from near closest approach are acquired at close range looking nearly perpendicular to the plume axis, where the time delay is sufficient to observe even slow-moving ejecta at altitude. Ejecta released at 2 m $s^{-1}$, for example, have climbed above 300 m in altitude. The images acquired after closest approach have Dimorphos obscuring the lowest portion of the plume once the impact site is behind the limb, and only the plume portion above the limb is imaged. The distant departure images are again viewing roughly along the plume axis, but now at a solar phase angle of about 120°.

The LICIACube images of the plume density structure and evolution provide information on the ejecta mass versus velocity distribution, because that distribution determines how much mass reaches a given altitude at a given time. The ejecta mass versus velocity distribution depends on the target physical properties, so that the observations of the plume spatial structure and evolution also constrain these properties and help determine $\beta$ (Cheng et al. 2020). As in the previous work, the present ejecta plume model uses point-source impact scaling laws (Housen & Holsapple 2011) to describe the mass versus velocity distribution, which is written as $M(v)$, the cumulative mass of ejecta released above the velocity $v$. Cheng et al. (2016) used this $M(v)$ from point-source scaling to calculate the momentum transfer efficiency $\beta$, giving an analytic approximation, which agreed with numerical simulation results to within 10% (Raducan et al. 2019).

The Housen & Holsapple (2011) point-source scaling laws are summarized in the Appendix B. The cumulative distribution $M(v)$ is given as a parametric equation in terms of the ejecta release radius $x$ measured horizontally from the impact point in the target surface. Specifically, the cumulative mass $M(x)$ released within radius $x$ is in Equation B2(b), and the ejecta release velocity $v(x)$ at radius $x$ is in Equation B2(a).

Figure 2 shows the DART impact ejecta mass–velocity distributions $M(v)$ from point-source scaling for three target cases, which will be the cases used to calculate the plume optical depth profiles in the next section. Table 3 shows the

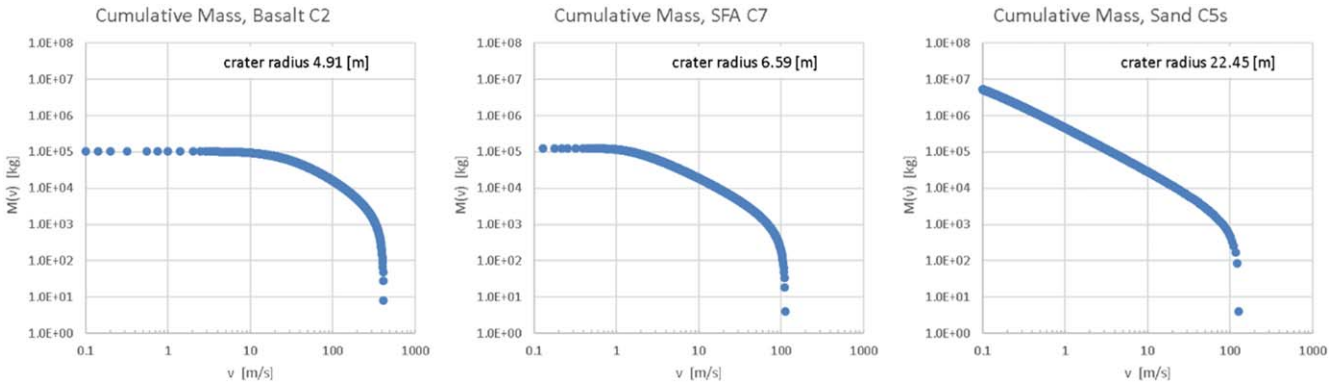


**Figure 2.** Cumulative mass $M$ ejected above velocity $v$, for three target cases from Housen & Holsapple (2011). Target cases Basalt C2 and SFA C7 are strength-controlled at high and moderate strength, respectively. Case C5 is gravity-controlled.

**Table 3**
DART Impact Outcomes from Point-source Scaling

| | Basalt C2 | SFA C7 | Sand C5 |
|---|---|---|---|
| Crater Radius $R$ (m) | 4.91 | 6.59 | 44.9 |
| Momentum Transfer Efficiency $\beta$ | 2.14 | 1.16 | 1.62 |
| Crater Growth Time (s) | 0.038 | 6.53 | 2883 |

crater radius and the momentum transfer efficiency from these same target cases, where the crater radius is given by Equations B1(a), (b) and $\beta$ is calculated by the method of Cheng et al. (2016), using the following DART impact parameters: impactor mass $m = 590$ kg and radius $a = 1.2$ m corresponding to density $\rho = 84.3$ kg m$^{-3}$, and impact velocity 6.15 km s$^{-1}$. For these parameters, the DART impact onto Dimorphos would be strength-controlled for a strength $Y > 3.5$ Pa. Hence with target case C5 where the strength is 1 Pa (see Appendix B, Table 4), the DART impact would be gravity-controlled. The crater radius in this case is large enough that target curvature may be important, with increased uncertainty on the crater size (Raducan & Jutzi 2021a, 2021b). With target cases C2 and C7, where the target strength is much larger at 30 MPa and 4 kPA, respectively, the DART impact crater would be strength-controlled and much smaller than the Dimorphos radius. The impact outcomes given in Table 3 differ slightly from those in Cheng et al. (2020), because of projectile parameter updates, most importantly a larger value for the projectile radius better describing the spacecraft structure (Raducan et al. 2022). Finally Table 3 shows the crater growth timescale for the three target cases, as given by point-source scaling (O'Keefe & Ahrens 1993; see Appendix B). This is the time to maximum growth of the crater diameter, which will be compared to times of LICIACube image acquisition in the next section.

The ejecta are assumed to be released from the impact point at a fixed ejection angle $\alpha$, nominally 45° to the target surface, filling the surface of a cone (sketched in Figure 1, also Figure 3) with ejection angles in the small range ($\alpha$, $\alpha + \delta\alpha$). The ejecta release from a single point neglects the variation in release points within the crater radius $R$ compared to the range to LICIACube, which is 1028 km at DART impact, decreasing to 51.2 km at closest approach. The fixed angle $\alpha$ is a simplification as ejection angles vary over roughly 40°–60° (Gulde et al. 2018; Luther et al. 2018), both because the ejection angle depends on the release radius from the central point of impact and because the ejection angle takes a range of values from any release radius.

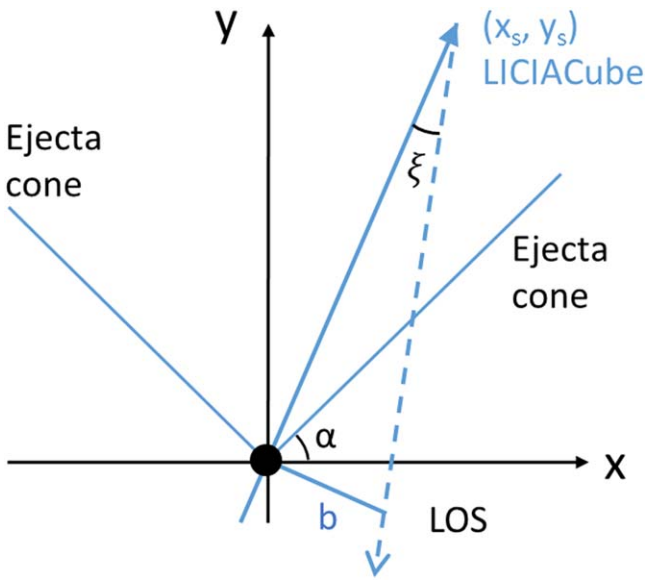


**Figure 3.** $x$–$y$ plane showing ejecta cone and ejection angle $\alpha$. The dashed arrow is the line of sight (LOS) from LICIACube at ($x_s$, $y_s$). LICIACube is inside the ejecta cone with LOS angle $\xi > 0$ and $b$ distance $> 0$, where $b$ is the distance in the plane of sky along the $\boldsymbol{x_b}$ direction of Figure 1.

A further simplification is made that only ejecta above the escape speed (~10 cm s$^{-1}$) are considered, as these ejecta make the dominant contribution to $\beta$ (Jutzi & Michel 2014; Cheng et al. 2016). The model represents these ejecta as being released on rectilinear trajectories at constant speed, an excellent approximation for ejecta that have not moved much more than a kilometer from the impact site. However, the time of ejecta release is accounted for as in point-source scaling (O'Keefe & Ahrens 1993), with the release time being a function of the release radius from the central point of impact (see Appendix B for details).

The ejecta plume optical depth is now calculated by an integration along the line of sight (LOS) from LICIACube. At the time of an image $t$ relative to the DART impact, the LOS for an image pixel intersects the ejecta cone once or twice (if twice, the two optical depth contributions are summed). If the LOS intersects the ejecta cone at radial distance $r$ from the impact site, the ejecta are released at velocity $v = r/t$. At the intersection point, the annular volume element is written as volume $= 2\pi r^2 \cos\alpha \ \ \delta r \ \delta\alpha$ and the path length through the

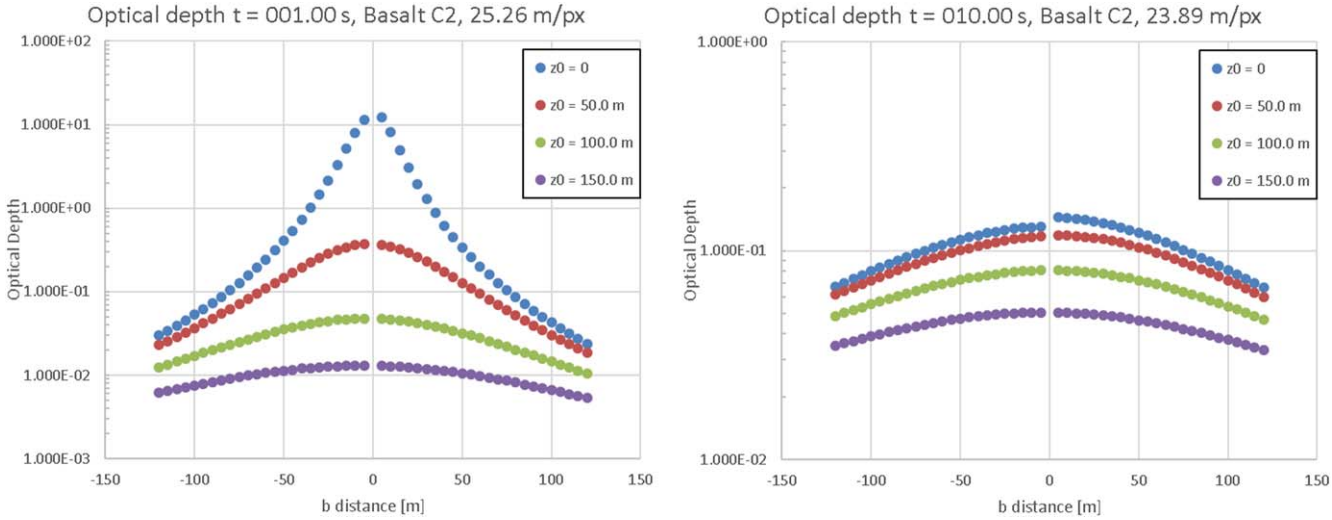


**Figure 4.** Ejecta plume extinction optical depths at two times, 1 and 10 s after DART impact, in target case basalt C2, showing rapid evolution and clearing of plume opacity for $|b| \lesssim 80$ m.

intersection is written as path $= \gamma\, r\, \delta\alpha$ where $\gamma > 1$ accounts for obliquity. The ejecta mass within the volume element is written as mass in $\delta r = \left|\frac{dM(v)}{dr}\right| \delta r$, which is found from a numerical differentiation of the cumulative mass distribution $M(v)$. The optical depth contribution from the intersection is then

$$\text{optical depth } \tau = \frac{\left|\frac{dM(v)}{dr}\right| \delta r\ \gamma\ r\ \delta\alpha}{2\pi r^2 \cos\alpha\ \delta r\ \delta\alpha} \left(\frac{\text{area}}{\text{mass}}\right) Q = \frac{\left|\frac{dM(v)}{dr}\right| \gamma}{2\pi r \cos\alpha} \left(\frac{\text{area}}{\text{mass}}\right) Q, \quad (1)$$

where the factor $\left(\frac{\text{area}}{\text{mass}}\right)$ is the total geometric cross section per unit mass of ejecta; this quantity is given by the particle size distribution, to be discussed below. The factor $Q$ is the scattering or extinction efficiency, relating the geometric cross section area to the scattering or extinction cross section, respectively.

To find the obliquity of the LOS through the ejecta cone, the ejecta cone surface sketched in Figure 1 is written as $y = \tan\alpha\sqrt{x^2 + z^2}$, and a normal vector to the cone at a point $(x, y, z)$ is $\left(\frac{xy}{x^2+z^2}, -1, \frac{zy}{x^2+z^2}\right)$. The LOS from LICIACube at position $(x_s, y_s, 0)$ to the cone intersection $(x, y, z)$ is written as the vector $(x - x_s, y - y_s, z)$. The obliquity is calculated from the reciprocal of the inner product of the normal vector and the LOS.

The plume optical depth is calculated on a grid of $(x, z)$ values chosen as follows (see Figure 3): $z = z_0$ is chosen, and the $x$ values are found corresponding to chosen values of the distance $b$, which determines the LOS angle $\xi$ from the direction to the impact site. The distance $b$ is also the abscissa plotted in the optical depth profiles of Section 3 and the profiles shown by Cheng et al. (2020). From Figure 3, the LOS slope is $A = \frac{y_s + x_s \tan\xi}{x_s - y_s \tan\xi}$, and the $x$ value at the cone intersection is found from

$$x^2 = \left(\frac{A(x - x_s) + y_s}{\tan\alpha}\right)^2 - z^2. \quad (2)$$

For the $x$ values corresponding to the chosen distances b and the chosen value for $z = z_0$, the $y$ values of the cone intersection are given by $y = \tan\alpha\sqrt{x^2 + {z_0}^2}$ and the radial distances $r = \sqrt{x^2 + y^2 + {z_0}^2}$.

The total cross sectional area per unit mass $\left(\frac{\text{area}}{\text{mass}}\right)$ is found from an assumed ejecta particle size distribution as in Cheng et al. (2020). An Itokawa size distribution is adopted, where the (differential) number of particles is $n(s) = 2.746 \times 10^5\ s^{-3.98}$ in the diameter range from $d_1 = 6.59 \times 10^{-4}$ m to $d_2 = 1$ m. The area of particles is $A_d = \int_{d_1}^{d_2} ds\ \pi s^2\, n(s)/4$ and the volume is $V_d = \int_{d_1}^{d_2} ds\ \pi s^3\, n(s)/6$, from which $\left(\frac{\text{area}}{\text{mass}}\right) = \frac{A_d}{\rho_g V_d} = 0.0981\ \text{m}^2\,\text{kg}^{-1}$ for an assumed particle density $\rho_g = 3000\,\text{kg m}^{-3}$. The adopted size distribution is consistent with boulder size distributions on Itokawa (Mazrouei et al. 2014; Tancredi et al. 2015) at the meter scale and larger, with the returned Itokawa sample particle size distribution above about a micrometer size (Nakamura et al. 2012; Cheng et al. 2020), and with impact experiments (Buhl et al. 2014).

## 3. LICIACube Plume Imaging Optical Depth Profiles

The optical depth profiles of $\tau$ versus the distance $b$ are calculated from Equation (1) and plotted in Figures 4–11, which show the extinction optical depth, that is, calculated assuming $Q = Q_e = 2$. The scattering and extinction efficiencies $Q_s$, $Q_e$ respectively depend not only on particle sizes but also on shape and composition (Fu & Sun 2001). For an initial examination of information that can be obtained from plume imaging by LICIACube, simplifications are adopted for $Q$. Namely, for estimating the obscuration of the target body surface as seen by LEIA through the plume, that is, for the extinction optical depth in the visible, the approximation $Q_e = 2$ is adopted bearing in mind that the assumed smallest particle size $d_1 = 6.59 \times 10^{-4}$ m is much larger than the wavelength (Hansen & Travis 1974). For estimating the brightness of the plume seen against the dark sky when the plume is optically thin, the rough estimate $I/F \sim 0.1\,\tau$ is adopted (Cheng et al. 2020), where $\tau$ is the optical depth shown in Figures 4–11, in cases where $\tau < 1$. This estimate of $I/F$,

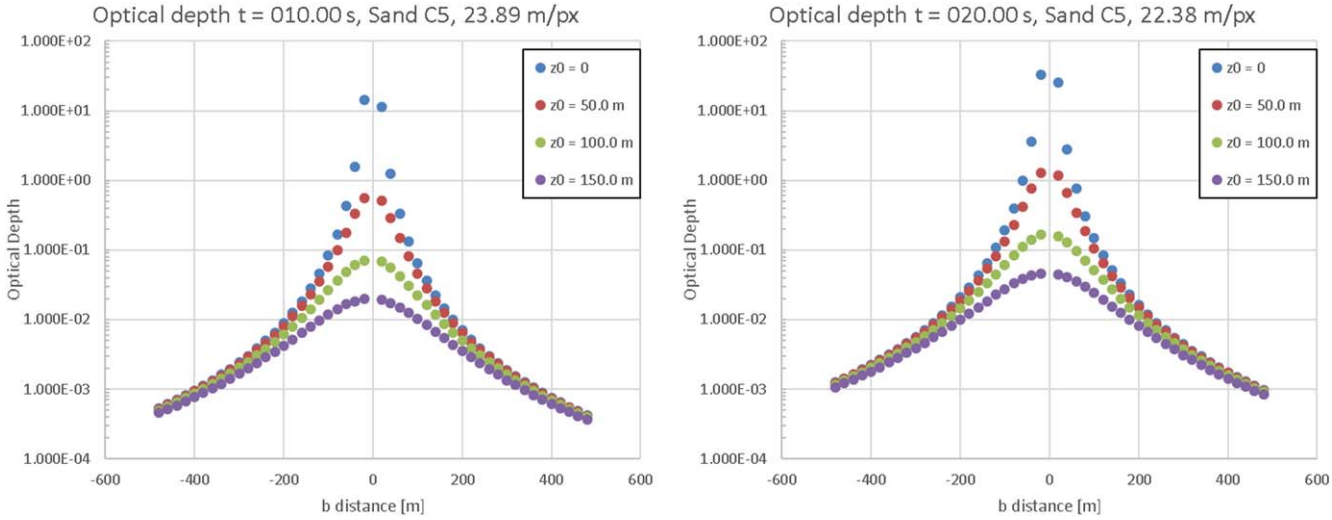


**Figure 5.** Ejecta plume extinction optical depths at two times, 10 and 20 s after DART impact, in target case sand C5, showing increase in the optical depth over this time interval for all $b$ distances plotted. LEIA image resolution at Dimorphos is indicated.

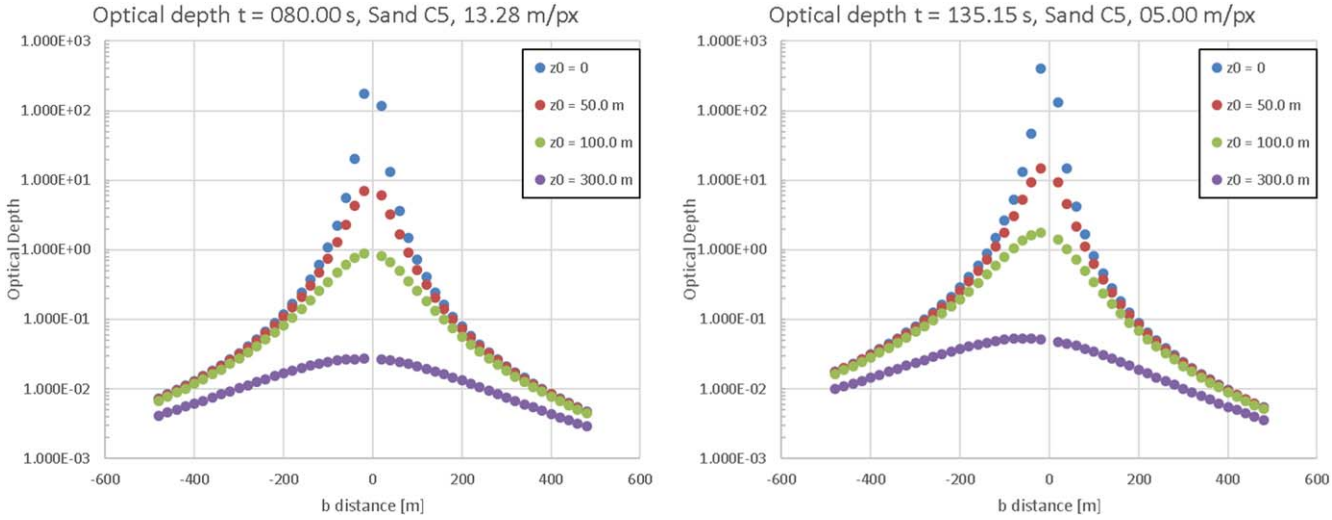


**Figure 6.** Ejecta plume extinction optical depths at two times, 80 and 135 s after DART impact, in target case sand C5, showing continued increases in optical depth. LEIA image resolution at Dimorphos is indicated.

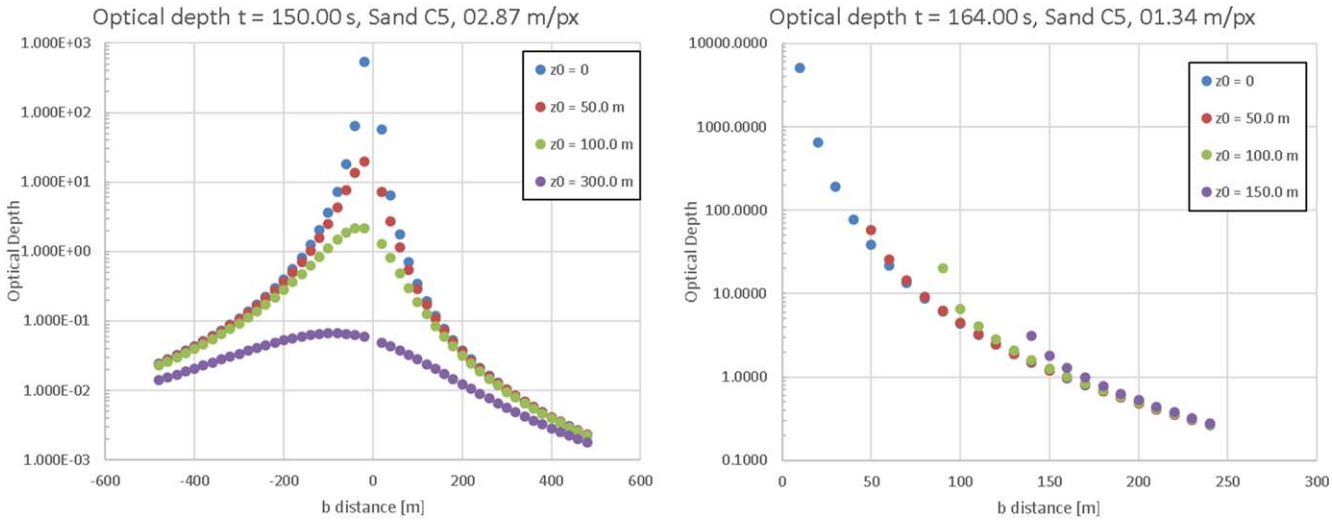


**Figure 7.** Ejecta plume extinction optical depths at 150 and 164 s after DART impact, in target case sand C5. At $t = 150$ s, there is a pronounced asymmetry in $\pm b$ just before cone crossing. At $t = 164$ s after cone crossing, ejecta plume is viewed from outside. LEIA image resolution is indicated.

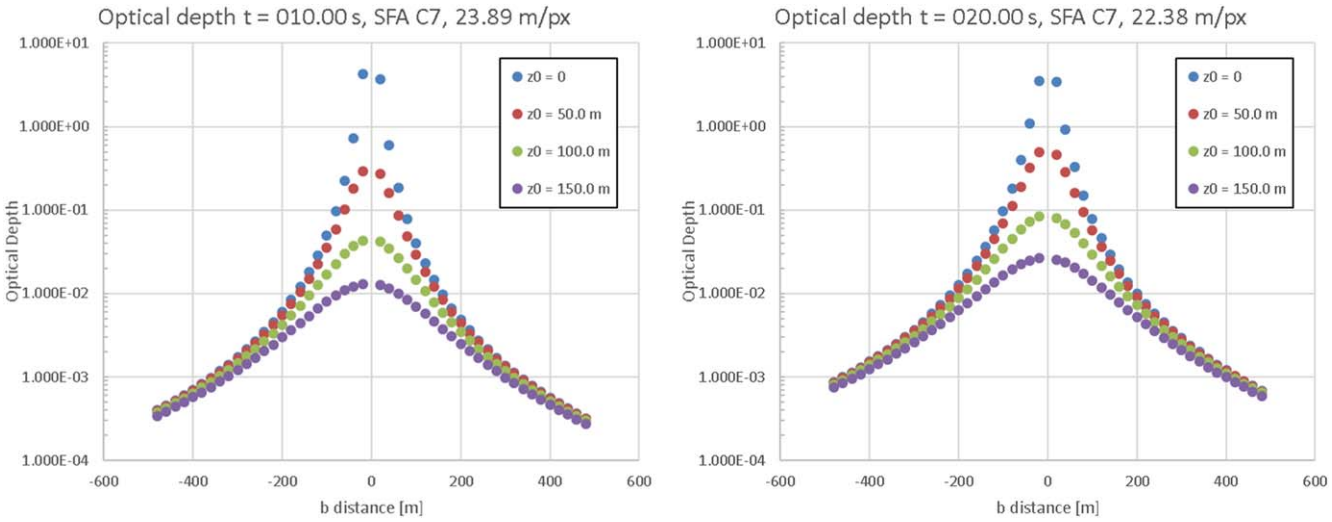


**Figure 8.** Ejecta plume extinction optical depths at two times, 10 and 20 s after DART impact, in target case SFA C7, showing an increase in the optical depth over this time interval at $b$ distances plotted. LEIA image resolution is indicated.

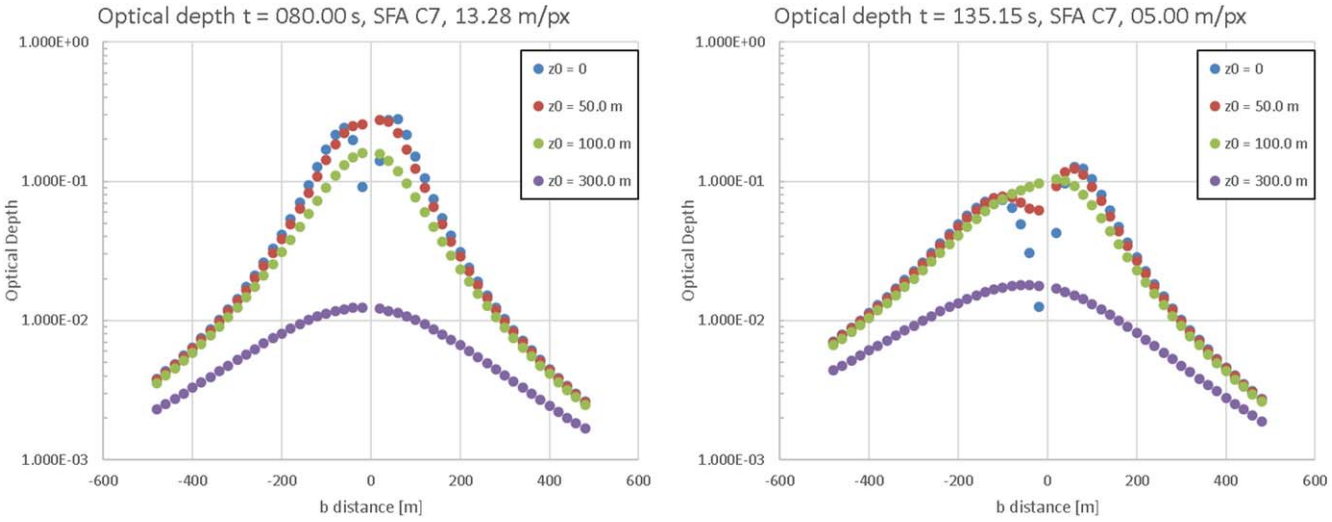


**Figure 9.** Ejecta plume extinction optical depths at two times, 80 and 135 s after DART impact, in target case SFA C7, showing clearing of plume opacity near the impact site vs. increases in the optical depth farther away in the plane of sky. Plume asymmetry is evident at the later time, 135 s. LEIA image resolution is indicated.

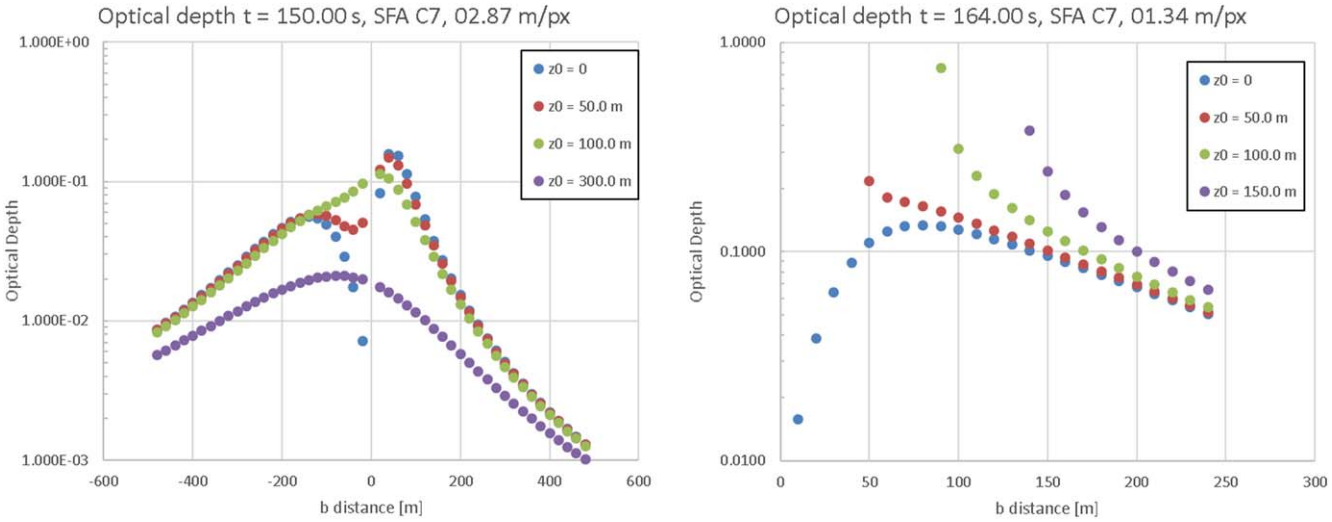


**Figure 10.** Ejecta plume extinction optical depths at two times, 150 and 164 s after DART impact, for SFA C7. At $t = 150$ s, there is pronounced asymmetry in $\pm b$ just before cone crossing. At $t = 164$ s after cone crossing, ejecta plume is viewed from outside. LEIA image resolution is indicated.

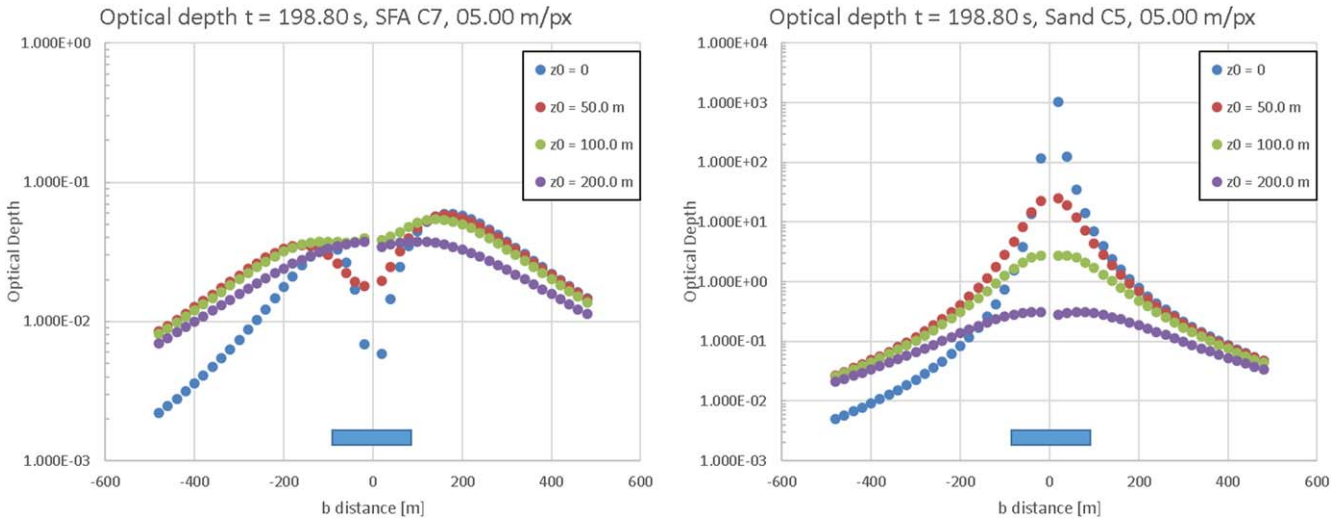


**Figure 11.** Ejecta plume extinction optical depths for SFA C7 and for sand C5 at time $t = 198.8$ s, after closest approach and looking back at Dimorphos. Plume is imaged above the limb of Dimorphos, at a 120° solar phase angle. The Dimorphos size is indicated by 160 m scale bars.

where $I$ is the scattered radiance and $\pi F$ is the solar irradiance, is equivalent to assuming a scattering efficiency $Q_s = 1.5$ with a phase function of 0.53 for plume particles large compared to an optical wavelength, observed at phase angles $\geqslant 60°$ (Hansen & Travis 1974). When the plume is optically thick, radiative transfer modeling is needed to account for multiple scattering to determine plume brightness. Multiple scattering is not considered in the present model.

Figures 4–11 compare the ejecta plume structure and temporal evolution as imaged by LICIACube for the three target cases of Table 3, one gravity-controlled and two strength-controlled. The spatial and temporal variations of the plume optical depth are compared for the target cases, and not the absolute magnitudes of the opacities, because the latter depend on particle size distribution determining $\left(\frac{\text{area}}{\text{mass}}\right)$ and on particle photometric properties determining $Q_e$ and $Q_s$. If the particle size distribution or photometric properties were changed from the nominal values assumed in the present model, the optical depth profiles would be shifted by a constant factor.

LICIACube imaging covers a limited range of solar phase angle. The distant approach images are near 60° phase angle (Figures 4, 5, and 8), the images near closest approach are near 90° (Figures 7, 10), and the departure images are near 120° (Figure 11).

Figure 4 shows plume extinction optical depth profiles for the first target case basalt C2, with high strength ($Y = 30$ MPa) and low porosity, at two times after the DART impact, $t = 1$ s and $t = 10$ s. At time $t = 1$ s, the LICIACube range from Dimorphos is 1021.5 km, and the LEIA image resolution is 25.2 m px$^{-1}$; at the later time $t = 10$ s, the range and the image resolution are 966.3 km and 23.9 m px$^{-1}$, respectively. This target case has high-velocity ejecta (see Figure 2): half the ejecta mass is released above 35.5 m s$^{-1}$; 10% of the mass is released above 134 m s$^{-1}$, and 90% of the mass is released above 10.3 m s$^{-1}$. Appendix B, Table 4 gives a complete listing of the target cases and scaling law parameters.

Figure 4 shows fast evolution at early times for target case basalt C2. By 10 s after the DART impact, clearing of ejecta plume opacity (decrease in the optical depth) is already evident close to the impact site within $|b| \lesssim 80$ m, but the optical depth is increasing at larger distances from the impact site. This is as would be expected for the $M(v)$ of basalt C2, where only a small mass fraction of ejecta is released at low enough velocity to remain below 80 m at $t = 10$ s. Most ejecta have already moved to higher altitude, and the result is that plume opacity decreases at low altitude. Also, at the early times shown in Figure 4, LICIACube is viewing the axisymmetric ejecta cone from close to its axis, and contours of constant optical depth are expected to be approximately circular. This expectation can be verified in Figure 4, where the optical depth is nearly the same at $(b, z_0) = (\pm 50$ m, 0) and $(b, z_0) = (0, 50$ m), and the same is true at $(\pm 100$ m, 0) and (0, 100 m).

Figures 5–7 show the optical depth profiles for target case sand C5 where the strength is low enough that the DART impact would be gravity-controlled (see Appendix B, Table 4). In target case sand C5, with very low strength ($Y = 1$ Pa) and moderate porosity ($\rho = 1510$ kg m$^{-3}$), one half of the ejecta mass is released above 16 cm s$^{-1}$; 10% of the mass is released above 64 cm s$^{-1}$, and 90% of the mass is released above 9.7 cm s$^{-1}$. In contrast to the other target cases shown in Figure 2, the cumulative mass $M(v)$ for sand C5 increases with decreasing $v$ down to below 10 cm s$^{-1}$. The significant ejecta mass fraction released at velocity under 1 m s$^{-1}$ means that, even near LICIACube closest approach $t \approx 167$ s, most of the ejecta mass has not yet climbed to 100 m altitude. Clearing of the plume optical depth at low altitude prior to the LICIACube closest approach would not be expected in this target case.

Figure 5 shows the plume optical depth profiles at two times, 10 and 20 s after DART impact, in target case sand C5. At the later time $t = 20$ s, the LICIACube range to Dimorphos and the LEIA image resolution are 904.9 km and 22.4 m px$^{-1}$, respectively. In Figure 5, the optical depth increases with time at all $b$ shown between $t = 10$ s and $t = 20$ s, as would be expected for a continually increasing $M(v)$ with decreasing $v$. This increasing optical depth contrasts with the clearing of opacity at low altitude seen in Figure 4 for the high-strength target case C2.

Additional differences between the optical depth profiles resulting from high- and low-strength targets are found from

comparison of Figures 4 and 5. In Figure 5 for sand C5 at time $t = 10$ s, the plume has optical depth $\tau > 1$ within ~40 m of the impact site (in the plane of sky at Dimorphos), and the optical depth drops rapidly to $\tau \approx 0.1$ within ~100 m of the impact site. In Figure 4 for basalt C2 at the same time $t = 10$ s, the peak optical depth is much less, with the maximum $\tau = 0.15$, and the optical depth decreases with the distance from the impact site much more gradually, dropping by about a factor of 2 out to distance 100 m in the plane of sky. In Figure 5 as in Figure 4, the optical depth contours in the plane of sky are nearly circular. The optical depths are nearly the same at $(b, z_0) = (\pm 50$ m, 0) and $(b, z_0) = (0, 50$ m), and also at $(b, z_0) = (\pm 100$ m, 0) and (0, 100 m).

Figure 6 shows optical depth profiles at later times during the approach, but still before cone crossing at $t = 158.6$ s. At $t = 80$ s, the LICIACube range from Dimorphos is 537 km, and the LEIA image resolution is 13.28 m px$^{-1}$; at the later time $t = 135$ s, the range and the image resolution are 202.4 km and 5.0 m px$^{-1}$, respectively. The optical depths continue to increase during this time interval for plane-of-sky distances out to ~400 m. By $t = 135$ s, the optical depth is $\tau > 1$ out to plane-of-sky distances over 100 m, larger than the 83 m radius of Dimorphos, and the plume may largely obscure Dimorphos from view.

By the later time $t = 135$ s in Figure 6, the profiles show an asymmetry between negative and positive $b$ values, as LICIACube approaches the ejecta cone crossing time. The asymmetry comes about because the LICIACube trajectory is $x_s = 51.2$ km and is offset from the asteroid (see Figure 1). Although the plume is axisymmetric in the present model, it is not viewed along the symmetry axis, and observed profiles are asymmetric between positive and negative $b$. However, the optical depth profiles are symmetric between positive and negative $z$.

In the Figure 7 profiles at $t = 150$ s, just before cone crossing, there is a more pronounced asymmetry in $\pm b$. For $z_0 = 0$, 50, 100 m the optical depths are an order of magnitude larger at $b = -200$ m than at $b = 200$ m. This asymmetry arises from two effects. First, the side of the ejecta cone closer to LICIACube, at positive $b$, is viewed at higher obliquity, which increases the optical path length. Second, the positive $b$ side closer to LICIACube views ejecta at higher altitude, implying higher-velocity ejecta. With the sand C5 ejecta distribution $M(v)$, the mass fraction of higher-velocity ejecta is strongly reduced. The second effect overcomes the first, leading to an overall reduction on the positive $b$ side. The $\pm b$ asymmetry depends on the shape of $M(v)$ and is therefore also diagnostic of the target properties.

The Figure 7 profiles at the later time $t = 164$ s, just after cone crossing and near LICIACube closest approach, show the ejecta cone viewed from the outside, on lines of sight roughly perpendicular to the cone axis that intersect the ejecta cone twice, generally at two different altitudes (see Figure 1). The two optical depth contributions are summed on these lines of sight. The optical depths climb steeply viewing the plume at small distances from the impact site, without any evidence of clearing of plume opacity at low altitudes. The plume is optically thick out to beyond 100 m altitude at $t = 164$ s for sand C5.

Figures 8–10 show the optical depth profiles in the target case SFA C7, which has a strength ($Y = 4$ kPa) that is high enough for the DART impact to be strength-controlled, versus the much lower strength, gravity-controlled case sand C5. The porosity for SFA C7 ($\rho = 1500$ kg m$^{-3}$) is nearly the same as for sand C5 (see Appendix B, Table 4), and these two cases compare primarily the effects of different target strengths on the plume structure and evolution arising from differences in the mass–velocity distribution $M(v)$. For SFA C7, $M(v)$ differs from that for basalt C2 in the generally lower ejecta velocities and in the different power-law slope (smaller $\mu$ reflecting higher porosity; see Appendix B, Table 4). In target case SFA C7, one half of the ejecta mass is released above 2.9 m s$^{-1}$; 10% of the mass is released above 8 m s$^{-1}$, and 90% of the mass is released above 1.3 m s$^{-1}$. Only a small mass fraction in SFA C7 is released below 1 m s$^{-1}$, and in the high-strength case basalt C2 a similarly small fraction is released below 10 m s$^{-1}$. The result is the clearing of plume opacity at low altitude observable by LICIACube before closest approach. However, in target case sand C5, the power-law region of $M(v)$ extends to below 10 cm s$^{-1}$, and 94% of the ejecta mass is released below 1 m s$^{-1}$. In this gravity-controlled case, the clearing of plume opacity at low altitude would not be expected before LICIACube closest approach.

Figures 8 shows the plume optical depth profiles at two times, 10 and 20 s after DART impact, in target case SFA C7, showing increases in the optical depth during this time interval at all $b$ plotted, with the exception of points $(b, z_0) = (\pm 20$ m, 0). The plot resolution of the optical depths in Figure 8 is 20 m, similar to the image resolutions indicated in the figure. The optical depth profiles calculated at 5 m resolution (not shown) reveal that clearing of plume opacity has already begun by $t = 20$ s, and that the $z_0 = 0$ profile peaks near $b = \pm 15$ m. However this clearing of opacity is not resolved in LEIA images. At the resolution of LEIA, the early time plume optical depth profiles are similar in the two low-strength target cases SFA C7 (Figure 8) and sand C5 (Figure 5), but both of these are qualitatively different from the high-strength target case basalt C2 at early times (Figure 4).

Figure 9 shows the optical depth profiles at later times during the approach, but still before cone crossing at $t = 158.6$ s. By $t = 80$ s, with a LEIA image resolution of 13.28 m px$^{-1}$, the clearing of opacity near the impact site is seen out to 50 m distance in the plane of sky, and clearing of opacity is seen out to 100 m distance by $t = 135$ s. However at larger distances >200 m in the plane of sky, the optical depths are increasing during this time interval. Because of the clearing of opacity that is seen in the profiles of Figure 9 for SFA C7, the optical depth profiles in this strength-dominated impact case are clearly distinguished from those for the gravity-controlled case, sand C5 in Figure 6, during the later time interval 80–135 s.

At the later time $t = 135$ s in Figure 9, the optical depth profiles display asymmetry in $\pm b$, where greater optical depth is seen for positive $b$ than for negative $b$. This asymmetry becomes more pronounced by $t = 150$ s in Figure 10, still before the cone crossing. It is noted that the asymmetry is such that optical depths are greater for positive $b$ than negative $b$, provided $|b| < 100$ m, opposite to the asymmetry shown in Figure 7 in the gravity-controlled case sand C5. However, for larger $|b|$ the asymmetry is of the same sign as in Figure 7, where optical depths are greater for negative $b$ than positive $b$. The differences in the $\pm b$ asymmetry further distinguish the strength-controlled case SFA C7 from the gravity-controlled case sand C5.

The Figure 10 profiles for SFA C7 at the later time $t = 164$ s, just after cone crossing and near LICIACube closest approach, show the ejecta cone viewed from the outside and once again indicate the clearing of plume opacity at low altitudes. This clearing of opacity seen in images near closest approach further distinguishes the strength-controlled case SFA C7 from the gravity-controlled case sand C5.

Figure 11 shows ejecta plume optical depths for two target cases, SFA C7 and sand C5, at time $t = 198.8$ s looking back at Dimorphos after closest approach. LICIACube continues its autonomous tracking of Didymos after closest approach and slews to obtain images of the nonimpact hemisphere and the ejecta plume above the limb of Dimorphos at 120° solar phase angle. Dimorphos is in front of the plume, and only the portions of the profiles above the limb are visible to LICIACube. The size of Dimorphos is indicated by scale bars in Figure 11. The optical depth profiles in Figure 11 at $t = 198.8$ s are usefully compared to those at $t = 135$ s in Figure 9 for SFA C7 and in Figure 6 for sand C5, all of which are at the same imager resolution 5 m px$^{-1}$. Comparison of the strength-controlled SFA C7 profiles in Figure 11 and in Figure 9 shows continued clearing of plume opacity in the $z_0 = 0$, 50, 100 m profiles within $|b| < 100$ m (much of this region is behind Dimorphos). However, $z_0 = 200$ m profiles for SFA C7 show increases in the optical depth from $t = 135$ s in Figure 9 to $t = 198.8$ s in Figure 11, with a much greater increase for positive $b$ than for negative $b$. Comparison of the gravity-controlled sand C5 profiles in Figures 11 and 6 shows the development of asymmetry in $\pm b$ and the continued lack of clearing of plume opacity. The asymmetry for sand C5 in Figure 11 is such that the optical depth is $\tau > 1$ in the $z_0 = 0$, 50 m profiles from $b = -80$ m to $b = +180$ m, and the $\tau > 1$ region in the $z_0 = 100$ m profile is found from $b = -60$ m to $b = +120$ m. The $\tau > 1$ region for sand C5 in Figure 11 is offset toward positive $b$. Finally the $z_0 = 200$ m profiles for sand C5 show increases in the optical depth from $t = 135$ s in Figure 6 to $t = 198.8$ s in Figure 11, with a much greater increase for positive $b$ than for negative $b$. This behavior is similar to that seen for SFA C7 in Figure 11; clearing of plume opacity for sand C5 has not yet developed out to distances in the plane of sky past 200 m.

## 4. Discussion and Conclusions

A full two-dimensional model of the impact ejecta plume optical depth as imaged by LICIACube extends the previous plume model developed by Cheng et al. (2020), which calculated the optical depth profiles along the image line at $z = 0$ connecting the impact site with the closest approach point of the LICIACube trajectory to Dimorphos, projected into the plane of sky. The present model calculates the optical depth profiles along image lines at arbitrary $z$ covering the full two-dimensional plume images. LICIACube images of the ejecta plume can discriminate the differences in plume structure and evolution that result from different target physical properties like the strength and porosity, because the plume images characterize the ejecta mass versus velocity distribution.

The models of ejecta plume opacity as imaged by LICIACube provide important information to determine the momentum transfer from the DART impact on Dimorphos. First is to determine the direction of the ejecta momentum from the LICIACube images, by finding the direction of the plume axis and characterizing asymmetry around this axis. This is important information to determine $\beta$, because the DART impact causes a three-dimensional momentum transfer, but the measured Didymos binary period change determines only one component of the velocity change (Cheng et al. 2018; Rivkin et al. 2021, and Appendix). Second, the plume optical depth profiles and their temporal evolution enable characterization of the ejecta mass versus velocity distributions and inference of target physical properties, so that gravity-controlled impacts can be distinguished from strength-controlled impacts with target strengths at least ~1 kPa. This information is important, because numerical simulations show that many distinct combinations of target physical properties like strength and porosity can yield very similar $\beta$ values, even for fixed DART impact conditions (Stickle et al. 2022). The constraints on target physical properties from LICIACube plume imaging contribute to understanding the momentum transfer from the DART impact.

The present models of ejecta plume opacity are subject to two major limitations. The first limitation arises from simplifications to the descriptions of ejecta and release trajectories: the ejecta are considered to be released from a fixed point ($x = 0$) and at a fixed ejection angle $\alpha$, so that all trajectories lie on the surface of a cone of infinitesimal thickness (the ejecta cone); the mass released at a given velocity and the time of release are obtained from point-source scaling laws; and the ejecta follow rectilinear trajectories. The second limitation arises from simplifications to geometric cross sections and optical properties of ejecta, affecting estimation of the plume extinction (obscuration of Dimorphos behind the plume) and plume brightness: the geometric cross section is found from the parameter $\left(\frac{\text{area}}{\text{mass}}\right)$ calculated assuming a power-law size distribution of spherical particles; the extinction efficiency is simplified to $Q_e = 2$ in modeling of the extinction optical depth (ejecta particles are large compared to an optical wavelength); and only a rough estimate of plume brightness is given for optically thin conditions. The model does not consider multiple scattering and does not predict plume brightness for optically thick conditions.

The ejection angle $\alpha$ is an observable that can be determined from LICIACube data in two ways. First the time of ejecta cone crossing by LICIACube can be inferred from plume images with $\pm b$ asymmetry, and the cone crossing time yields a determination of $\alpha$. Second, the ejection angle $\alpha$ is directly observable in LICIACube plume images obtained from outside the cone. For plume images obtained near or after the cone crossing, the ejection angle $\alpha$ does not need to be inferred simultaneously with the inference of target material cases, but an observed value of $\alpha$ can be used to discriminate target cases. However, at earlier times, the ejection angle may differ by 10° from the $\alpha$ value measured near or after cone crossing (Luther et al. 2018; Raducan et al. 2022). This variation in $\alpha$ should be considered to infer target physical properties.

Also important to consider is the possible effect of inhomogeneous structures at the scale of the DART impact. In the Hayabusa 2 SCI impact experiment on Ryugu (Arakawa et al. 2020), such structures including a 5 m boulder adjacent to the crater led to the splitting of the ejecta cone into four crater rays. Recent laboratory experiments and numerical studies (Ormö et al. 2021; Raducan & Jutzi 2021b) suggest that boulders within the target affect the final crater diameter by only ~10%, but they affect the impact ejecta cone by locally inhibiting ejecta escape to regions downstream of boulders,

thereby forming rays. In such a picture, the present ejecta plume model for a homogeneous target, creating a full ejecta cone, can be applied to the ejecta seen within crater rays (if rays are observed to form), considering that ejecta are missing between the rays owing to the presence of boulders. If the ejecta cone is split to form crater rays, the $\pm b$ asymmetry may be difficult to observe.

Figures 4–11 illustrate how the plume optical depth profiles can distinguish high- and low-strength target cases, ranging from very strong and nonporous to very weak and porous, including the very-low-strength (1 Pa) sand C5 case with a gravity-controlled DART impact, and two cases with a strength-controlled impact at moderately low (4 kPa) and high (30 Mpa) strength, SFA C7 and basalt C2, respectively. The low-strength target cases SFA C7 and sand C5 have nearly the same density ($\sim$1500 kg m$^{-3}$). The ejecta plume optical depth profiles can distinguish between all of these cases. It is emphasized that the observables from plume images that are proposed to discriminate between target material cases and constrain physical properties involve the spatial variations of the optical depth and the temporal evolution, but not the absolute values of the optical depth.

Specific observables in plume images to distinguish target material cases include the time at which clearing of ejecta is seen over the impact site. This time is earlier for the stronger, less porous targets, as illustrated by the impact cases considered in Figures 4–11: the clearing times are $\sim$10 s for basalt C2, $\sim$80 s for SFA C7; but for the gravity-controlled case, clearing does not begin before closest approach at $t = 167$ s. If clearing has started, the distance at which the optical depth reaches a maximum is another useful observable in profiles obtained near closest approach from outside the cone, when LICIACube images the plume along lines of sight almost perpendicular to the plume axis as in Figures 7 and 10. If clearing has not started, the optical depth increases continually toward Dimorphos. The plume images after closest approach, when LICIACube has turned around to view the plume in forward scattering above the limb of the target body, provide additional information on $\pm b$ asymmetry and on the extent of plume optical depth clearing to constrain target physical properties by distinguishing between target material cases. However, if the particle size distribution parameters and $\left(\frac{\text{area}}{\text{mass}}\right)$ are too different from the nominal values of Section 3, then the plume opacity may be reduced to the extent that any clearing of opacity would not be observable.

The timescales of crater growth are shown in Table 3 for the three target material cases in order to make comparison with the times of LICIACube observations. For the high-strength target case basalt C2, the crater growth is completed and all ejecta are released before the first LICIACube observation time considered. For the target case SFA C7, which is weaker but still strength-controlled for DART impact, the crater growth time occurs during distant approach before cone crossing, and plume images obtained after completion of crater growth can show clearing of plume opacity over the impact site. The clearing of plume opacity means not only that crater growth has been completed, but also that sufficient time has elapsed for the last released, and slowest-moving, ejecta to have reached a sufficient altitude to be observed. However, in the lowest-strength target case sand C5, with a gravity-controlled DART impact, the crater growth time is much longer than any of the LICIACube observation times. In this case, no clearing of plume opacity is observed, and all LICIACube observations are obtained before all expected ejecta mass is released.

The ejecta plume is seen in LICIACube approach images in front of and obscuring the lit surface of Dimorphos. For modeling the plume extinction optical depth in the visible, the approximation $Q_e \sim 2$ is made bearing in mind that the assumed smallest particle size $d_1 = 6.59 \times 10^{-4}$ m is much larger than the wavelength. LICIACube images with plume obscuring the surface of Dimorphos can be compared to pre-impact images of Dimorphos from DART to determine the plume extinction optical depth, although a radiative transfer model is needed if the plume is optically thick. In the present model with its assumed size distribution down to submillimeter particles, Figures 4–10 indicate that, in all three target cases considered, at least one limb of Dimorphos is visible through the plume at low optical depth before LICIACube closest approach. In the sand C5 gravity-controlled case, the plume becomes optically thick out to substantial distances from the impact site (e.g., Figure 7), but with pronounced $\pm b$ asymmetry the plume can be optically thin over one limb. The significance of observing a limb of Dimorphos through the ejecta plume is that this observation enables determination of the plume optical depth as was done for Deep Impact at comet 9P/Tempel 1 (Kolokolova et al. 2016). If the plume optical depth can be determined, then the ejecta particle size distribution is determined while fitting optical depth profiles to the ejecta plume observations, better constraining the target physical properties.

We thank NASA for support of the DART mission at JHU/APL under Contract # NNN06AA01C, Task Order # NNN15AA05T. SDR thanks the EU Horizon 2020 program, grant 870377. E.D. and V.D.C. thank the Italian Space Agency.

## Appendix A
## Momentum Transfer Efficiency

When a kinetic impactor of mass $m$ strikes a target at velocity $\boldsymbol{U}$, the momentum transferred to the target of mass $M$, written as $M\Delta\boldsymbol{v}$, can exceed the incident momentum $m\boldsymbol{U}$ because of momentum carried away in a backward direction by impact ejecta. In general, the vector momentum transfer $M\Delta\boldsymbol{v}$ is not collinear with the incident momentum vector $m\boldsymbol{U}$ because of the ejecta momentum vector, which is not antiparallel to the incident direction, but is affected by either or both of: (1) the local surface inclination to the incident direction as discussed by Feldhacker et al. (2017), or (2) topography or a blocky surface at the impact site (Stickle et al. 2018, 2020). The momentum transfer efficiency $\beta$ is defined by Feldhacker et al. (2017)

$$M\Delta\boldsymbol{v} = m\boldsymbol{U} + m(\beta - 1)(\boldsymbol{n} \cdot \boldsymbol{U})\boldsymbol{n}, \tag{A1}$$

where the first term on the right is the incident momentum and the second term is the net momentum of escaping impact ejecta, which is along the unit vector $\boldsymbol{n}$. This definition of $\beta$ can be reexpressed as the ratio of the components along $\boldsymbol{n}$ of both the momentum transfer and the incident momentum vectors, or

$$\beta = \frac{M(\boldsymbol{n}\cdot\Delta\boldsymbol{v})}{m(\boldsymbol{n}\cdot\boldsymbol{U})}. \tag{A2}$$

If the surface is locally flat and homogeneous, and the incident direction is not too far from the surface normal, then the ejecta momentum direction $\boldsymbol{n}$ can be approximated by the local surface normal unit vector $\boldsymbol{n_s}$ at the impact site (Feldhacker et al. 2017). Equation (A1) for $\beta$ can be rewritten in terms of the surface normal $\boldsymbol{n_s}$, the offset vector $\boldsymbol{\epsilon}$ of the ejecta momentum perpendicular to $\boldsymbol{n_s}$ defined by $\boldsymbol{n} = (\boldsymbol{n_s} + \boldsymbol{\epsilon})(\boldsymbol{n} \cdot \boldsymbol{n_s})$, and the unit vector $\boldsymbol{e_T}$ along the Dimorphos orbital motion, yielding (Rivkin et al. 2021)

$$\Delta \boldsymbol{v} \cdot \boldsymbol{e_T} = \frac{m}{M}[\beta(\boldsymbol{U} \cdot \boldsymbol{n_s})\boldsymbol{n_s} + \boldsymbol{U} - (\boldsymbol{U} \cdot \boldsymbol{n_s})\boldsymbol{n_s} + (\beta - 1)(\boldsymbol{U} \cdot \boldsymbol{n_s})\boldsymbol{\epsilon}] \cdot \boldsymbol{e_T}, \quad \text{(A3)}$$

where $\Delta \boldsymbol{v} \cdot \boldsymbol{e_T}$, the velocity change along the orbital motion, is determined by the period change observations.

## Appendix B
## Point-source Scaling Model of DART Impact

The ejecta plume model is based upon the point-source impact scaling laws of Housen & Holsapple (2011) as applied by Cheng et al. (2016) to the DART impact. A spherical impactor of mass $m$ and radius $a$ is incident normally at velocity $U$. The crater radius $R$ is nondimensionalized by target density $\rho$ and impactor mass $m$, and the combination $R\left(\frac{\rho}{m}\right)^{1/3}$ is expressed in terms of the dimensionless scaling parameters $\pi_2 = \frac{ga}{U^2}$ and $\pi_3 = \frac{Y}{\rho U^2}$ in the gravity- or strength-controlled impact cases, respectively. Here $\pi_2$ is the gravity-scaled size, with $g$ the target surface gravity; and $\pi_3$ is the strength parameter (the ratio of material strength and inertial stresses) with target impact strength $Y$ and target density $\rho$. In the gravity-controlled case, the crater radius $R$ is given by

$$R\left(\frac{\rho}{m}\right)^{1/3} = H_1\left(\frac{\rho}{\delta}\right)^{\frac{2+\mu-6\nu}{3(2+\mu)}}\left(\frac{ga}{U^2}\right)^{-\frac{\mu}{2+\mu}} \quad \text{(B1a)}$$

In the strength-controlled case the crater radius $R$ is given by

$$R\left(\frac{\rho}{m}\right)^{1/3} = H_2\left(\frac{\rho}{\delta}\right)^{(1-3\nu)/3}\left(\frac{Y}{\rho U^2}\right)^{-\mu/2}. \quad \text{(B1b)}$$

The dimensionless scaling parameter $\mu$ depends on target properties and lies in the range $1/3 < \mu < 2/3$, where $\mu = 1/3$ is the momentum scaling limit, and $\mu = 2/3$ is the energy scaling limit. The scaling parameter $\nu$ enters via the ratio of target to projectile densities $\rho/\delta$, and $\nu$ is empirically about 0.4 for any target material. The normalization of the crater size (and thus total ejecta mass) is given by $H_1$ or $H_2$ for gravity or strength scaling, respectively.

The ejecta plume mass versus velocity distribution is described following Housen & Holsapple (2011). The speed of ejecta $v$ that are released at radial distance $x$ from the central point of impact, when nondimensionalized by the incident velocity $U$, is

$$\frac{v}{U} = C_1\left[\frac{x}{a}\left(\frac{\rho}{\delta}\right)^{\nu}\right]^{-1/\mu}\left(1 - \frac{x}{n_2 R}\right)^{p}. \quad \text{(B2a)}$$

The impact is at normal incidence, and ejecta are released on ballistic trajectories. The mass $M$ ejected from within $x$, which is also the mass ejected above the corresponding speed according to Equation (B2a), is

$$\frac{M}{m} = \frac{3k}{4\pi}\frac{\rho}{\delta}\left[\left(\frac{x}{a}\right)^3 - {n_1}^3\right]. \quad \text{(B2b)}$$

The ejecta mass versus velocity distribution is defined implicitly by Equations B2(a) and (b) and has a cutoff at high ejecta velocity, corresponding to the cutoff at small $x = n_1 a$ in Equation B2(b), and additionally a cutoff at low ejecta velocity corresponding to large $x = n_2 R$ from Equation B2(a). Parameters $C_1$ and $k$ normalize the ejecta velocities and ejecta mass, respectively. The times of ejecta release are also a function of $x$ (O'Keefe & Ahrens 1993), according to

$$t_{\text{release}} = \frac{a}{U}\left(\frac{x}{a}\right)^{(1+\mu)/\mu}. \quad \text{(B3)}$$

The crater growth times (O'Keefe & Ahrens 1993) are for strength-controlled cratering

$$t_{\text{growth}} = 0.33\left(\frac{a}{U}\right)\pi_3^{-\frac{1+\mu}{2}} \quad \text{(B4a)}$$

and for gravity-controlled cratering

$$t_{\text{growth}} = 1.8\left(\frac{a}{U}\right)\pi_2^{-\frac{1+\mu}{2+\mu}}. \quad \text{(B4b)}$$

In Table 3, cases basalt C2 and SFA C7 are strength-controlled, while case sand C5 is gravity-controlled.

Empirical values for these parameters, based on fitting to ejecta velocity distributions from laboratory experiments

**Table 4**
Target Cases for DART Impact Ejecta Modeling

| Target[a] | Porosity | $\mu$ | $C_1$ | $k$ | $H_1$, $H_2$ | $p$ | $a$ (mm) | $U$ (m s$^{-1}$) | $\delta$ (kg m$^{-3}$) | $\rho$ (kg m$^{-3}$) | $Y$ (MPa) |
|---|---|---|---|---|---|---|---|---|---|---|---|
| Basalt C2 | ~0 | 0.55 | 1.5 | 0.3 | 1.1 | 0.5 | 1.6 | 6200 | 2700 | 3000 | 30 |
| WCB C3 | 20% | 0.46 | 0.18 | 0.3 | 0.38 | 0.3 | 3.6 | 1860 | 2700 | 2600 | 0.45 |
| SFA C7 | 45% | 0.4 | 0.55 | 0.3 | 0.4 | 0.3 | 7 | 1900 | 930 | 1500 | 0.004 |
| PS C8 | 60% | 0.35 | 0.6 | 0.32 | 0.81 | 0.2 | 8.7 | 1800 | 940 | 1200 | 0.002 |
| Sand C5 | 35% | 0.41 | 0.55 | 0.3 | 0.59 | 0.3 | 3.9 | 6770 | 1220 | 1510 | $10^{-6}$[b] |

**Notes.**
[a] WCB = weakly cemented basalt; SFA = sand/fly ash; PS = perlite/sand; C2, C3, C5, C7, and C8 are labels used by Housen & Holsapple (2011); in strength-controlled cases, $\upsilon = 0.4$, $n_1 = 1.2$, $n_2 = 1$.
[b] Gravity-controlled case C5 of Housen & Holsapple (2011), where $\upsilon = 0.4$, $n_1 = 1.2$, $n_2 = 1.3$, with assumed strength $Y = 1$ Pa.

(Housen & Holsapple 2011), are shown in Table 4 for four target cases with strength-controlled impacts, labeled C2, C3, C7, and C8, and one additional gravity-controlled case labeled C5. Numerical simulations (Prieur et al. 2017) have determined appropriate scaling parameters for additional target materials spanning a wide range of target properties.

The target cases in Table 4 are arranged in descending order of target strength, from the strong intact basalt case that is unlikely to apply (Cheng et al. 2016), to moderate strength cases with $Y$ of a few kPa for which the DART impact would be strength-dominated, and to a gravity-controlled case that may apply if Dimorphos is nearly strengthless. Assuming a Didymos density of 2.1 g cm$^{-3}$ for the target body (Rivkin et al. 2021) and a projectile radius $a = 1.2$ m, the DART impact onto Dimorphos would be strength-controlled for a target strength $Y > 3.5$ Pa. Hence with the four target cases C2, C3, C7, C8 the DART impact would be strength-controlled, and with target case C5 the impact would be gravity-controlled for the assumed target strength of 1 Pa. The other target case parameters $\mu$, $\rho$, $C_1$, $k$, $H_1$, $H_2$ are the same as those obtained by Housen & Holsapple (2011) for their gravity-controlled case C5, the rationale being that these parameters apply to any strength value low enough for the terrestrial laboratory sand target impact to be gravity-controlled. The strength of 1 Pa is also low enough for the DART impact to be gravity-controlled.

A target strength as high as that of lunar regolith, ~0.1–1 kPa, would already be high enough that strength scaling would apply at the scale of the DART impact, which is typical for asteroid mitigation by kinetic impact (Holsapple & Housen 2012; Cheng et al. 2016). The upper surface strength on Comet 67P inferred from the Philae landing (Biele et al. 2015) was estimated as ~1 kPa, although geologic features on Comet 67P (overhangs) required tensile/shear strengths of only 10–20 Pa (Thomas et al. 2015). Cometary meteoroid strengths (from bolide breakup in the upper atmosphere) are also typically ~1 kPa (Trigo-Rodriguez & Llorca 2007). However, the Hayabusa 2 artificial impact on Ryugu, a 2 kg impactor at 2 km s$^{-1}$ (a much smaller scale than DART), produced a gravity-controlled crater (Arakawa et al. 2020), suggesting a target strength possibly on the order of 0.1–1 Pa.

## ORCID iDs

Andrew F. Cheng https://orcid.org/0000-0001-5375-4250
S. D. Raducan https://orcid.org/0000-0002-7478-0148
Angela M. Stickle https://orcid.org/0000-0002-7602-9120

## References

Arakawa, M., Saiki, T., Wada, K., et al. 2020, Sci, 6486, 67
Biele, J., Ulamec, S., Malbaum, M., et al. 2015, Sci, 349, 6247
Bruck Syal, M., Owen, J. M., & Miller, P. L. 2016, Icar, 269, 50
Buhl, E., Sommer, F., Poelchau, M., Dresen, G., & Kenkmann, T. 2014, Icar, 237, 131
Cheng, A. F., Michel, P., Jutzi, M., et al. 2016, P&SS, 121, 27
Cheng, A. F., Rivkin, A. S,, Michel, P., et al. 2018, P&SS, 157, 104
Cheng, A. F., Stickle, A. M., Fahnestock, E. G., et al. 2020, Icar, 352, 113989
Dotto, E., Della Corte, V., Amoroso, M., et al. 2021, P&SS, 199, 105185
Feldhacker, J. D., Bruck Syal, M., Jones, B. A., et al. 2017, JGCD, 40, 2417
Fu, Q., & Sun, W. 2001, ApOpt, 40, 1354
Gulde, M., Kortmann, L., Ebert, M., et al. 2018, MAPS, 53, 1696
Hansen, J. E., & Travis, L. D. 1974, SSRv, 16, 527
Holsapple, K., & Housen, K. 2012, Icar, 221, 875
Jutzi, M., & Michel, P. 2014, Icar, 229, 247
Housen, K., & Holsapple, K. 2011, Icar, 211, 856
Kolokolova, L., Nagdimunov, L., A'Hearn, M., King, A., & Wolff, M. 2016, P&SS, 133, 76
Luther, R., Zhu, M.-H., Collins, G., & Wuennemann, K. 2018, MAPS, 53, 1705
Michel, P., Cheng, A., Küppers, M., et al. 2016, AdSpR, 57, 2529
Mazrouei, S., Daly, M. G., Barnouin, O. S., Ernst, C. M., & DeSouza, I. 2014, Icar, 229, 181
Michel, P., Kueppers, M., Sierks, H., et al. 2018, AdSpR, 62, 2261
Nakamura, E., Makishima, A., Moriguti, T., et al. 2012, PNAS, 109, E624
O'Keefe, J., & Ahrens, T. 1993, JGR, 98, 17011
Ormö, J., Raducan, S. D., Luther, R., et al. 2021, EPSC 15, EPSC2021–587
Prieur, N. C., Rolf, R., Luther, R., et al. 2017, JGR, 122, 1704
Raducan, S., Davison, T. M., Luther, R., & Collins, G. S. 2019, Icar, 329, 282
Raducan, S., & Jutzi, M. 2021a, LPSC, 52, 1900
Raducan, S. D., & Jutzi, M. 2021b, EPSC 15, EPSC2021–623
Raducan, S. D., Jutzi, M., Davison, T. M., et al. 2022, IJIE, 162, 104147
Rivkin, A. S., Chabot, N. L., Stickle, A. M., et al. 2021, PSJ, 2, 173
Stickle, A. M., Bruck Syal, M., Cheng, A. F., Collins, G. S., et al. 2020, Icar, 338, 113446
Stickle, A. M., Burger, C., Caldwell, W., et al. 2022, PSJ, submitted
Stickle, A. M., Rainey, E., Owen, J. M., et al. 2018, LPSC, 49, 1576
Tancredi, G., Roland, S., & Bruzzone, S. 2015, Icar, 247, 279
Thomas, N., Sierks, H., Barbaieri, C., et al. 2015, Sci, 347, aaa0440
Trigo-Rodríguez, J. M., & Llorca, J. 2007, MNRAS, 372, 655